Dielectric-dependent hybrid functional calculations on the electronic band gap of 3*d* transition metal doped SnS_2 and their optical properties

Bhagyashri Devaru Bhat
Department of Physics, Indian Institute of Science Education and Research, Pune 411008, India

(Received 30 January 2022; revised 28 April 2022; accepted 5 May 2022; published 20 May 2022)

This paper is a computational investigation of the electronic band gap and optical properties of SnS_2 and 3*d*-series transition metal doped SnS_2 systems. The SnS_2 crystal is a nonmagnetic indirect band gap semiconductor both in bulk and in the monolayer limit. The transition metal substitution at Sn site induces magnetism inside the crystal. Therefore studying its doping by 3*d*-series transition metals is essential from an application perspective. We use the dielectric-dependent hybrid functionals of *ab initio* calculations for computing the electronic band gap. The dielectric-dependent hybrid computations rely on the electronic static dielectric constant. In these calculations, we iteratively update the dielectric constant and exchange parameter from one another until the convergence. As a result, we present a range of possible band gap values. Specifically, we determine the lower and upper bounds of possible experimental band gap values for all these doped systems. Further, we explore the optical properties of each doped system in the monolayer and bulk forms. We discuss the absorption spectra, optical constants, and exciton binding energy of all the doped systems. We conclude that the transition metal doped SnS_2 is a good candidate for optoelectronic device applications.

DOI: 10.1103/PhysRevB.105.195205

I. INTRODUCTION

Layered metal dichalcogenides (LMDs) are found in nature as bulk crystals with van der Waals interactions connecting the layers. These are promising materials for field effect devices, memory devices, and energy storage, etc. Monolayers of them can be extracted via experimental techniques. The first monolayer to be produced experimentally is graphene [1]. Other layered materials of the form MX_2, where M = Ti, Hf, Zr and X = S, Se, Te [2–11] as well as the transition metal (TM) dichalcogenides MoS_2 [12–15], WS_2 [16,17], WSe_2 [18,19], and NbS_2 [20], are exceedingly promising materials due to their applications in electrical, optical, and magnetic fields.

As a metal dichalcogenide, SnS_2 originates from the MX_2 or CdI_2 crystal type [21]. The chemical stability of SnS_2 crystal makes it a nontoxic, nonflammable, affordable, and earth-abundant material that can resist water and air. The layered structure of SnS_2 allows one to synthesize it in a single layer. The single layer provides a large surface area for solar energy absorption and active sites for chemical reactions. The optical properties of the SnS_2 crystal are well studied. Also SnS_2 is an earth-abundant visible-light photocatalyst [22], making it a good candidate for Li-ion battery electrode [23,24], gas sensors [25], and field emitters [26]. The exfoliated nanomembranes of SnS_2 exhibit a high FET on/off ratio exceeding 2×10^6 and a carrier mobility of $\sim 1\ cm^2V - 1s^{-1}$ [27]. High-performance top-gated field-effect transistor along with the integrated logic circuits have been fabricated [28] in 2013, using monolayer SnS_2 crystals. Thus, SnS_2 will be a top candidate for next-generation electronic gadgets.

SnS_2 shows *n*-type electrical conductivity with a maximum dark value of $1.3 \times 10^{-2} cm^{-1}$, and activation energy of 0.14 eV with a wide band gap of 2.3 eV [29]. Thus a complete solar cell structure is built using SnS_2 crystal [29]. These findings imply that SnS_2, a layered semiconductor with a wide band gap, will be a nanoelectronic basis material, particularly as a supplement to graphene-based materials with very small or no band gap. SnS_2 is an indirect gap semiconductor in bulk and the monolayer limit, with a wide band gap of 2.2–2.43 eV. Therefore, a band gap narrowing process is required for applications such as solar cells. Narrowing it to nearly 1.5 eV and then maintaining the higher absorption coefficient is essential [30–32]. Attempts are made using defect engineering [33–36] and impurity doping [37,38] for reducing the band gap. Transition metal doping of the SnS_2 crystal in monolayer or bulk environments make its band gap fall below the band gap of pristine SnS_2 crystal.

Electronic properties of materials profoundly influence electronic, optoelectronic, and spintronic device applications. However, predicting electronic properties accurately with theoretical methods is a complex problem. Theoretical predictions do not match the experimental values very well. Thus computational methods play a major role.

In this regard, density functional theory [39] (DFT) is one of the popular methodologies that provides a good balance between accuracy and computation efficiency. The electronic band gap calculations using DFT involve exchange-correlation functionals such as local density approximation (LDA) [40], semilocal generalized gradient approximation (GGA) [41], and hybrid functionals [42–44]. Among these functionals, hybrid functionals are highly accurate [45,46]. They are the refined approximations to the exchange-correlation energy functional. In these hybrid approximations, part of the exact exchange is derived using the

Hartree-Fock theory, and the rest by density functional approximations (DFA). Hybrid functionals are classified using the Hartree-Fock exchange admixtures. They are short-range, long-range, or full-range separation. The effective nonlocal potential in the generalized Kohn-Sham formalism [47–49] is determined by

$$v_{\mathrm{GKS}} = v_H(r) + v_{xc}(r, r') + v_{\mathrm{ext}}(r), \tag{1}$$

where v_H is the Hartree potential, v_{xc} is the exchange-correlation potential, and v_{ext} is the external potential of the nuclei. Also v_{xc} can be expressed as

$$v_{xc} = v_x^{\mathrm{HF}} + v_x^{\mathrm{DFA}} + v_c(r), \tag{2}$$

where v_x^{HF} and v_x^{DFA} represent the exact exchange potentials corresponding to the Hartree-Fock and density functional approximations, respectively. $v_c(r)$ is the correlation potential.

$$v_x^{\mathrm{HF}} = v_x^{\mathrm{SR-HF}} + v_x^{\mathrm{LR-HF}}, \tag{3}$$

$$v_x^{\mathrm{DFA}} = v_x^{\mathrm{SR-DFA}} + v_x^{\mathrm{LR-DFA}}. \tag{4}$$

The terms represent the short-range and long-range part of the exact exchange potentials corresponding to the Hartree-Fock and the density functional approximations.

$$\begin{aligned} v_{xc} = {} & \alpha v_x^{\mathrm{SR-HF}}(r, r'; \omega) + (1-\alpha) v_x^{\mathrm{SR-DFA}}(r; \omega) \\ & + \beta v_x^{\mathrm{LR-HF}}(r, r'; \omega) + (1-\beta) v_x^{\mathrm{LR-DFA}}(r; \omega) \\ & + v_c(r), \end{aligned} \tag{5}$$

where α and β are mixing parameters for short-range and long-range exchange potentials. ω is the range separation parameter that separates the short-range and the long-range Hartree-Fock exchange potentials. Hartree-Fock exchange potentials are expressed as [50,51]

$$v_x^{\mathrm{LR-HF}}(r, r'; \omega) = -\sum_{i=1}^{N_{occ}} \phi_i(r)\phi_i^*(r') \frac{erf(\omega|r-r'|)}{|r-r'|}, \tag{6}$$

$$v_x^{\mathrm{SR-HF}}(r, r'; \omega) = -\sum_{i=1}^{N_{occ}} \phi_i(r)\phi_i^*(r') \frac{erfc(\omega|r-r'|)}{|r-r'|}. \tag{7}$$

Here ϕ_i are single-particle occupied electronic orbitals, erf and $erfc$ are error function and complimentary error functions, respectively. The Coulomb potential [42] is expressed as

$$\frac{1}{|r-r'|} = \frac{erfc(\omega|r-r'|)}{|r-r'|} + \frac{erf(\omega|r-r'|)}{|r-r'|}. \tag{8}$$

With a fixed mixing parameter, α and β the hybrids are called global-hybrid functionals. The hybrid functionals where the mixing parameter changes with material-dependent properties are known as local hybrid functionals.

When $\beta = 0$, the equation (5) becomes

$$\begin{aligned} v_{xc}(r) = {} & \alpha v_x^{\mathrm{SR-HF}}(r, r'; \omega) + (1-\alpha) v_x^{\mathrm{SR-DFA}}(r; \omega) \\ & + v_x^{\mathrm{LR-DFA}}(r; \omega) + v_c(r). \end{aligned} \tag{9}$$

These are the short-range hybrid functionals, e.g., HSE06 [52–54], here $\alpha = 0.25$ and $\omega = 0.11$ bohr^{-1}. When $\beta \neq 0$, then these are the long-range hybrid functionals, e.g., CAM-B3LYP functionals [55,56] where $\beta = 0.65$, $\alpha = 0.19$, $\omega = 0.33$ bohr^{-1}. The full-range hybrid functionals are with $\alpha = \beta$. For full-range hybrid functionals we have,

$$\begin{aligned} v_{xc}(r) = {} & \alpha v_x^{\mathrm{SR-HF}}(r, r'; \omega) + (1-\alpha) v_x^{\mathrm{SR-DFA}}(r; \omega) \\ & + \alpha v_x^{\mathrm{LR-HF}}(r, r'; \omega) + (1-\alpha) v_x^{\mathrm{LR-DFA}}(r; \omega) \\ & + v_c(r), \end{aligned} \tag{10}$$

$$\begin{aligned} v_{xc}(r) = {} & \alpha \left[v_x^{\mathrm{SR-HF}}(r, r'; \omega) + v_x^{\mathrm{LR-HF}}(r, r'; \omega) \right] \\ & + (1-\alpha) \left[v_x^{\mathrm{SR-DFA}}(r; \omega) + v_x^{\mathrm{LR-DFA}}(r; \omega) \right] \\ & + v_c(r), \end{aligned} \tag{11}$$

$$v_{xc}(r) = \alpha v_x^{\mathrm{HF}}(r, r') + (1-\alpha) v_x^{\mathrm{DFA}}(r) + v_c(r). \tag{12}$$

In our calculation, DFA refers to PBE functional. For the full-range hybrid functionals such as PBE0 [57] we have $\alpha = 0.25$. These hybrid functionals are known for their remarkable accuracy in predicting the band gap of bulk and two-dimensional (2D) materials comparable with experimental values. However, they are computationally expensive.

The electronic dielectric constant, ϵ_s is known to be a reliable screening parameter for understanding the exact exchange potential in nonmetallic systems. Marques *et al.* [58], Shimazaki and Asai [51,59–61], and Refacly-Abramson [62] reported that the electronic static dielectric constant of a nonmetallic system represents the effective screening of the exact-exchange potential, v_x^{screened}. Shimazaki and Asai calculated the band structure of Diamond using the screened Fock exchange method [63] in which they have utilized the Bechstedt model [64] for dielectric function and simplified it in the form of screened Fock exchange,

$$v_x^{\mathrm{screened}} = \left(1 - \frac{1}{\epsilon_s}\right) \left[v_{\mathrm{SR-}X}^{erfc} \right] + \frac{1}{\epsilon_s} v_x^{Fock}. \tag{13}$$

They have calculated the band gap of Diamond using the self-consistent screened Hartree-Fock exact exchange potential, which is in agreement with the experiment. Nevertheless, exactly how much exchange rate was involved in their calculation is not specified.

In a semiconductor system, the static dielectric constant, ϵ_∞ facilitates effective screening. Marques [58] *et al.* reported that the static dielectric constant calculated using the PBE functional, $\epsilon_\infty^{\mathrm{PBE}}$ could be related to the mixing parameter of the full-range hybrid functional as

$$\alpha = \frac{1}{\epsilon_\infty^{\mathrm{PBE}}}. \tag{14}$$

On the other hand using self-consistent scheme, Shimazaki and Asai [65,66] evaluated the relation

$$\alpha = \frac{1}{\epsilon_\infty}, \tag{15}$$

for both short-range and full-range screened hybrid functionals. Koller *et al.* [67] reported that in self-consistent short-range hybrid functionals the mixing parameter is inversely proportional to the static dielectric constant of the system. In recent publications, several authors have proposed introducing α as an adjustable parameter into solids to reproduce the experimental band gap [68–72].

In our computations, initially, the self-consistency loop is triggered by a guess for α, which ranges between 0 and 1; the estimate determines the exact amount of exchange included in the exchange-correlation potential expression. In this dielectric-dependent hybrid functional (DDHF) calculation, the static dielectric constant is calculated with HSE06 and PBE0 functionals based on the initial guess of α as 25%. In the first iteration of HSE06 and PBE0 calculation, exchange parameter is $\alpha = 25\%$. The inverse of the static dielectric constant calculated in the first iteration is taken as the exchange parameter for the next iteration. These steps are repeated until the static dielectric constant, and hence the band gap converges. Convergence is reached when the consecutive difference between the calculated static dielectric constant, $\epsilon_\infty < 0.01$. When the static dielectric constant converges, the band gap also converges. These self-consistent HSE06 and PBE0 calculations are performed to find the band gap of bulk and monolayer SnS_2 and all the transition metal-doped systems. We also use the inverse of the static dielectric constant obtained by the PBE functional to do a one-run hybrid functional computation to estimate the band gap.

II. COMPUTATIONAL DETAILS

First principles calculations [73] are performed by using Vienna *ab initio* simulation package (VASP) [74,75]. The electron-ion interactions in these calculations were carried by projector augmented wave (PAW) [76,77] pseudopotentials. Since SnS_2 is a layered van der Waals material, the van der Waals interaction is involved in the DFT calculation.

The bulk and ML-SnS_2 crystals are relaxed using Perdew, Burke, and Enzerhof (PBE) generalized gradient approximation (GGA) [41] with *D*3 [78], optB86b [79] vdw functions to calculate the ground-state lattice parameters, respectively. While doing the calculations, atomic positions are optimized using the conjugate-gradient method with a force convergence criterion of 10^{-3} eV/Å and a tight energy convergence criterion of 1×10^{-8} eV. Cutoff energy of 400 eV is used. The Brillouin zone sampling of bulk and ML-SnS_2 was employed by Monkhorst-Pack [80] k grid of size $21\times21\times13$ and $21\times21\times1$, respectively. The electronic band gap values are estimated using the short-range, i.e., Heyd-Scuseria-Ernzerhof (HSE06) [52–54] and full-range, i.e., PBE0 [44] screened hybrid functionals with 25% exchange for the initial guess. A supercell of size $2\times2\times1$ is considered. One of the Sn atoms is replaced by each transition metal atom. The top view of the supercell doped with the transition metal atom is shown in Fig. 1. A self-consistent hybrid scheme is used for calculating the electronic part of the static dielectric constant. Each time, a fraction of the exact exchange of screened hybrid functional is calculated by the inverse of ϵ_∞. In this calculation, the LOPTICS tag in VASP employs the Kramers-Kronig transformation to separate the real part of the frequency-dependent dielectric function. The static dielectric constant is calculated using this code, and the local field effects are neglected to reduce the computational cost.

For bulk systems, the average of the dielectric constants along the x, y, and z axes is considered. For monolayers the dielectric constant is calculated using the relation

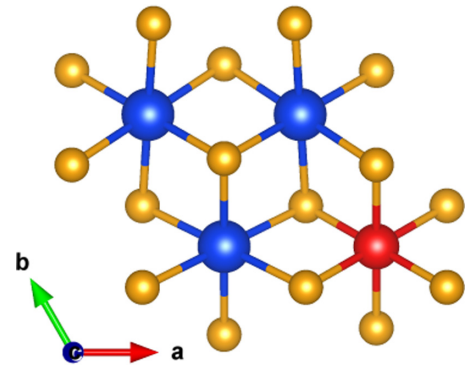

FIG. 1. Top view of SnS_2 crystal doped with transition metal atom. Blue, yellow, and red balls represent Sn, S, and transition metal atom, respectively.

$$\varepsilon_{2D} = \tfrac{1}{3}(2\varepsilon_{2D,\parallel} + \varepsilon_{2D,\perp}) \tag{16}$$

by eliminating the vacuum contribution. Where $\varepsilon_{2D,\parallel}$ and $\varepsilon_{2D,\perp}$ are the in-plane and out-of-plane dielectric constants of the proper 2D material. It is taken from the simple capacitor combinations of series and parallel connections of the slab-vacuum model proposed in Ref. [81].

III. RESULTS AND DISCUSSION

A. Structural stability

It is important to calculate the formation energy of each transition metal doped SnS_2 both in the bulk and monolayer form to explore the stability of the systems. The formation energy of the TM-doped systems are calculated using the relation [82,83],

$$E_{\text{form}} = E_{\text{doped}} - E_{\text{pristine}} - n\mu_{\text{TM}} + n\mu_{Sn}. \tag{17}$$

Here E_{doped} and E_{pristine} are the energies of transition metal doped and pristine systems, respectively. n is the number of Sn atoms replaced with transition metal atom. μ_{TM} and μ_{Sn} are the chemical potentials of the transition metal and Sn atom, respectively. For the pristine SnS_2 crystal the chemical potentials of Sn and S should satisfy [84]

$$\mu_{Sn} + 2\mu_S = \Delta E_f(SnS_2), \tag{18}$$

where $\Delta E_f(SnS_2)$ is the enthalpy of formation of SnS_2. Formation energy of such reaction is given by [85],

$$E_{\text{form}}(SnS_2) = \mu_{SnS_2} - \mu_{Sn,\text{bulk}} - 2\mu_{S,\text{bulk}}, \tag{19}$$

where $\mu_(SnS_2)$ is the energy per unit cell of the SnS_2 crystal. $\mu_{Sn,\text{bulk}}$ and $\mu_{S,\text{bulk}}$ are the energy per atom of the bulk Sn and bulk S crystal structure. The formation energy of bulk and ML SnS_2 are calculated as -1.48 and -0.95 eV/atom, respectively. Several thermodynamic constraints are applied to the chemical potentials to avoid the formation of elemental phases (Sn, S, and TM atom) and the secondary phases by TM atom with S atom [84]. The constraints applied to the chemical

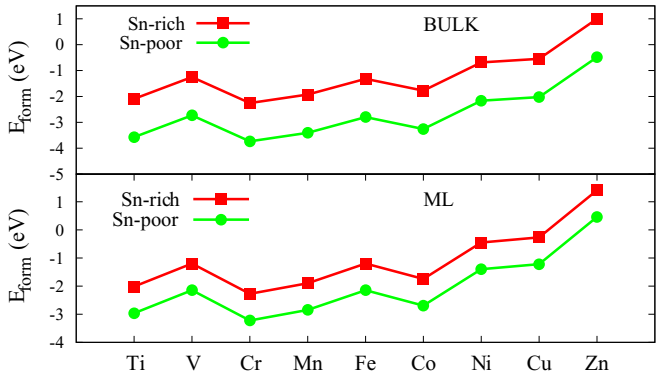

FIG. 2. Formation energy of transition metal doped bulk and ML-SnS_2.

potentials are [84],

$$\mu_{Sn} < 0, \mu_S < 0, \mu_{\mathrm{TM}} < 0, \tag{20}$$

$$n\mu_{\mathrm{TM}} + m\mu_S \leqslant \Delta E_f(TM_nS_m), \tag{21}$$

where $\Delta E_f(TM_nS_m)$ is the enthalpy of formation for the secondary phase TM_nS_m. The chemical potentials of TM atoms are calculated using the equations (20) and (21). The secondary phases constraining the TM atom chemical potentials are given in the Supplemental Material [86]. Since SnS_2 has two types of atoms Sn and S, we need to find the formation energies both in Sn-rich (S-poor) and Sn-poor (S-rich) experimental growth conditions. These conditions are based on the chemical potentials of the individual atoms. In Sn-rich and Sn-poor conditions μ_{Sn} is given by [85],

$$\mu_{Sn}^{Sn-\mathrm{rich}} = \mu_{Sn,\mathrm{bulk}}, \tag{22}$$

$$\mu_{Sn}^{Sn-\mathrm{poor}} = \mu_{Sn,\mathrm{bulk}} + \Delta E_f(\mathrm{SnS_2}). \tag{23}$$

The maximum allowed chemical potential of TM atom is considered to calculate the formation energy of each doped system in Sn-rich and Sn-poor conditions [84]. All the potential secondary phases of TM atoms and bulk phases of Sn and S atoms are taken from Materials Project [87], and their energies are calculated using VASP.

Figure 2 shows the formation energy of transition metal doped bulk and ML-SnS_2 in the Sn-rich and Sn-poor conditions. Here the green line (Sn-poor) falls below the red (Sn-rich) line. This indicates the lower formation energy in the Sn-poor (S-rich) condition than in Sn-rich (S-poor) condition in all the transition metal doped systems. Hence Sn-poor (S-rich) condition is the favorable condition to incorporate the transition metal atoms into SnS_2 crystal. As a result, the impurities Ti, V, Cr, Mn, Fe, Co, Ni, Cu, and Zn are comparatively easy to integrate into the SnS_2 crystal at the Sn site in Sn-poor (S-rich) condition. Therefore, further calculations are performed based on substitutional doping at the Sn site by the transition metal atom.

B. Electronic properties

Bulk SnS_2 crystal is a 2H polytype, it has hexagonal crystal structure with the space group of $P\bar{3}m1$ [89,90,94]. The six

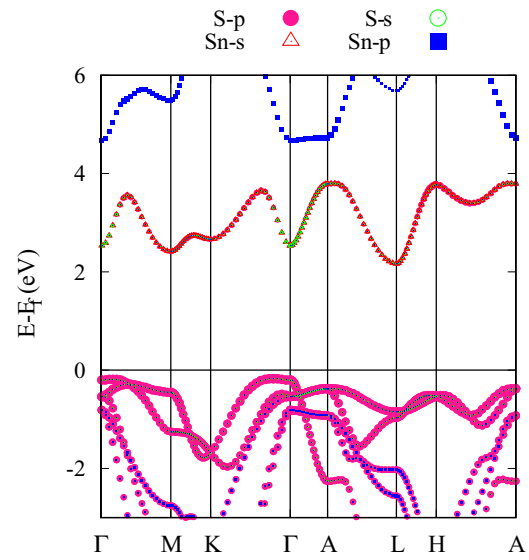

FIG. 3. Orbital projected band structure of bulk SnS_2 calculated using HSE06 functional with 25% exchange.

sulfur ligand field octahedrally surrounds the central Sn atom with Sn-S bond length of 2.60 Å. The calculated in-plane and transverse lattice parameters using vdw-D3 functionals are 3.64 Å and 5.98 Å, respectively. These values are in agreement with the other theoretical work [88] where $a = 3.69$ Å and $c = 5.98$ Å. Note that the single-crystal XRD [89] also has the parameters $a = 3.649$ Å and $c = 5.899$ Å. Monolayer SnS_2 crystallizes to the same space group whose top view and side views are same as the bulk SnS_2. The in-plane lattice parameter is found to be 3.68 Å using PBE functional and the Sn-S bond length is 2.59 Å. The band structure of pristine bulk SnS_2 is shown in Fig. 3. This shows, bulk SnS_2 has indirect gap nature like bulk MoS_2. In bulk MoS_2, the indirect gap appears due to the in-plane electronic transition. This transition happens from valence band edge at Γ point to conduction band edge between Γ and K point. In bulk-SnS_2, even though it is indirect, the valence band edge is near Γ point and conduction band edge is out of plane, at L point.

Valence band edge in bulk MoS_2 emerges from out-of-plane S-p_z and Mo-d_{z^2} orbitals, whereas conduction band edge is from S-p_x, p_y, p_z, and Mo-d_{xy}, $d_{x^2-y^2}$, d_{z^2} orbitals [95]. In bulk SnS_2, valence band edge originates from the S-p_y and S-p_x orbitals, conduction band edge is from Sn-s and S-p_x orbitals. Near the Fermi level, valence bands are mostly composed of S-p_x, p_y, p_z orbitals with a small amount of Sn-s, p_x, p_y, p_z orbitals. The conduction bands are composed of Sn-s and S-p_x, p_y, p_z orbitals very near to the Fermi level. Sn-p_x, p_y,p_z orbitals influence the conduction band far from the Fermi level. The fundamental (indirect) band gap calculated using HSE06 functional with D3 and optB86 corrections are 2.22 and 2.35 eV, respectively, for the exchange fraction of $\alpha = 25\%$. They are in agreement with the various research works shown in Table I. An experimental band gap value is 2.25 eV [92], Greenaway and Nitsche showed the value 2.21 eV [21] and Lokhande gave the value to be 2.35 eV [96]. Our band gap values are comparable with these experimental values. The direct gap calculated at L and M points is 2.66 eV and

TABLE I. Relaxed lattice parameters (a, b, and c), Sn-S bond length $d_{\mathrm{Sn-S}}$, direct E_g^{dir} and indirect band gap E_g^{in}, values of bulk and monolayer SnS_2 calculated using PBE, PBE-D3, and PBE-optB86b functionals, respectively. The HSE06 and PBE0 band gap values are calculated using PBE (D3 and optB86b) relaxed lattice parameters.

System	PBE $a=b$ (Å)	c (Å)	$d_{\mathrm{Sn-S}}$ (Å)	E_g^{in} (eV)	E_g^{dir} (eV)	HSE06 E_g^{in} (eV)	HSE06 E_g^{dir} (eV)	PBE0 E_g^{in} (eV)	PBE0 E_g^{dir} (eV)
BULK-SnS_2	3.64 (3.69) [88] (3.649) [89]	5.98 (5.98) [88] (5.899) [89]	2.60 (2.62) [88]	1.41	1.92[L]	2.22(D3) 2.35(optB86b) (2.18) [90] (2.07) [91] (2.28) [22] (2.25) [92]	2.66[L], 2.5[M] (D3) (2.88)[L] [91] (2.56)[M] [22] (2.61)[L] [90]	2.83 (optB86b)	3.36 [M] (optB86b)
ML-SnS_2	3.68 (3.68) [93]	-	2.59 (2.59) [93]	1.45	1.69[M]	2.43 (2.41) [90]	2.64 [M] (2.68)[M] [90]	3.11	3.41[M]

2.5 eV, respectively. The PBE0+optB86b functional gives the gap of 2.83 eV. This is higher than the calculated theoretical and experimental gaps.

In the case of monolayer MoS_2, both valence band edge and conduction band edge originate at the K point. This makes it as direct gap semiconductor. In this case, valence band edge is composed of Mo-d_{xy}+d_{x2-y2}, S-p_x+p_y orbitals and conduction band edge is of Mo-d_z^2, S-p_x+p_y orbitals [95]. Similar to MoS_2, indirect to direct gap transition occurs from bulk to monolayer limit in all of the transition metal dichalcogenides. However, this phenomenon does not occur in the case of SnS_2. In monolayer SnS_2, valence band edge originates near Γ point from the S-p_x and S-p_y orbital, whereas conduction band edge originates at M point from the Sn-s and S-p_x orbitals. This makes it an indirect gap semiconductor. The band structure is shown in Fig. 4. S-p_x, p_y orbitals dominate the valence bands near Fermi level, with Sn-p_x, p_y and s orbitals contributing only slightly. Sn-s, p_x, p_y orbitals make up the majority of the conduction bands, with a little proportion of S-p_x, p_y orbitals. The experimental band gap is 2.29 eV [97]. The HSE06 functionals with $\alpha = 25\%$ have shown the band gap of

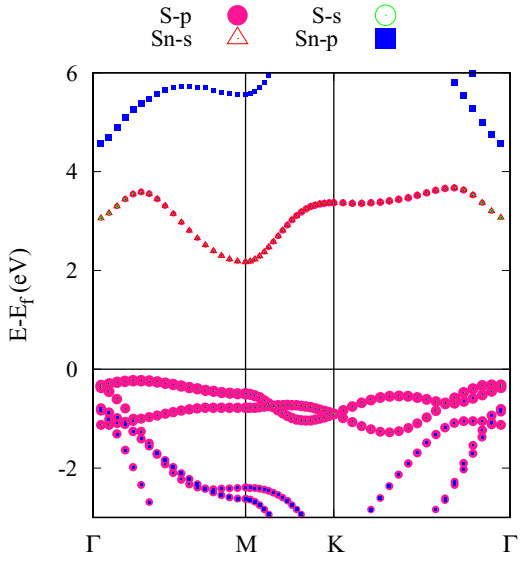

FIG. 4. Orbital projected band structure of monolayer SnS_2 calculated using HSE06 functional with 25% exchange.

2.43 eV. This is comparable with the other theoretical works shown in Table I. But the band gap of 3.11 eV calculated by PBE0 with $\alpha = 25\%$ overestimates the other theoretical and experimental band gap values. The direct gap calculated at the M point using HSE06 is 2.64 eV. Bulk (2.35 eV) and monolayer (2.43 eV) limit show that SnS_2 has a wider band gap compared to transition metal dichalcogenides. This is in contrast with phosphorene [98,99], where the layer thickness greatly influences the band gap.

C. Importance of DDHF calculation

The dielectric constant is equivalent to effective screening in semiconductor systems, as discussed in Sec. I. The mixing parameter is inversely related to the static dielectric constant in hybrid functionals. This fact is investigated for a variety of materials [51,58–62,100]. Instead of randomly choosing the exchange percentage value, the DDHF allows one to manually calculate the value of the exchange parameter based on the inverse static dielectric constant. The self-consistent steps performed by incorporating the exchange parameters into hybrid functionals provide the band gap values until convergence is reached. Band gap remains unchanged when the dielectric constant and exchange parameter converges. These iterations highlight how the band gap values change depending on the dielectric constant of the system and how it depends on the exchange parameter. In this sense, DDHF is not only important in calculating the range of band gap values but also provides the converged band gap value and minimal exchange percentage a system can have. There is no fixed value for the exchange percentage in the hybrid DFT calculations. One can easily understand this by considering the TiS_2 example. Finding the experimentally matchable band gap of 1T-TiS_2 using theoretical methods was a challenge for DFT calculations. We have first examined the band gap calculation of a bulk 1T-TiS_2. According to some tests, it has either semiconducting [101] or semimetallic [102] behavior. Klipstein and Friend [103] found that TiS_2 is a semiconductor with a gap of 0.18 ± 0.06 eV, Greenway and Nische [21] found that it is a semiconductor with a band gap of 1–1.12 eV by the optical measurement. Using angle-resolved photoemission studies (ARPS) Chen *et al.* [101] and Barry *et al.* [104] found a band gap of about 0.3 ± 0.2 eV. Using photoemission experiments, Shepherd and Williams [105] determined a band

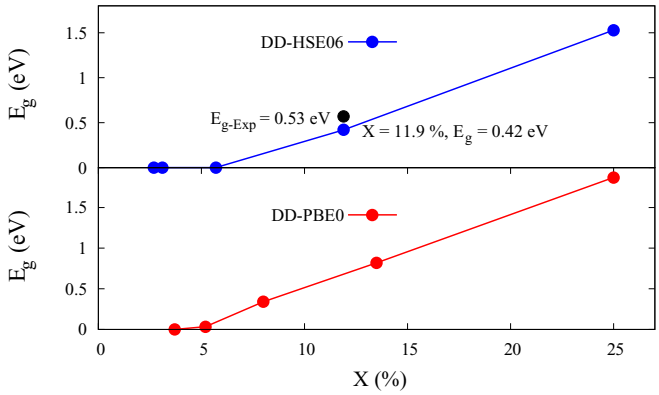

FIG. 5. Dielectric-dependent HSE06 and PBE0 band gap values of 1T-TiS_2.

gap of less than 0.5 eV. A band gap of 2 eV was estimated using the pseudopotential approach [102]. By employing the linearized augmented plane wave (LAPW) method [106], augmented spherical wave (ASW) method [107], the linear muffin-tin orbital (LMTO) method [108–110], and the full-potential (FP)-LAPW method [111,112] have claimed that TiS_2 displays semimetallic behavior. Using resistivity measurements [113,114], several experiments have concluded that TiS_2 shows metallic behavior.

The latest experiment on TiS_2 utilizing angle-resolved photoelectron spectroscopy (ARPES) [115] verifies the semiconducting nature with a band gap of 0.53 eV, while the HSE06 calculation with 20% exchange yields a band gap of 0.4 eV [115]. Our band structure computations utilised LDA, GGA, and meta-GGA (SCAN) functionals and revealed the metallic nature. HSE06 and PBE0 with $\alpha = 25\%$ yield band gaps of 1.53 eV and 1.87 eV, respectively, overestimating the ARPES band gap of 0.53 eV [115]. Finally, our DDHF calculations gave 0.42 eV for the 11.9% exchange and 0.34 eV for the 8% exchange, respectively, after which the TiS_2 system reaches a metallic phase, which is shown in Fig. 5. The band gap of 0.42 eV calculated with the 11.9% exchange of DD-HSE06 now matches the gap of 0.4 eV estimated by other theory work [115], as well as the experimental band gap of 0.53 eV [115]. This demonstrates that the experimental band gap value is calculated for the exchange value of 11.9% rather than 25%. DDHF has calculated the experimental matchable band gap value despite the system gaining the metallic phase. This confirms that a system's fundamental band gap or experimental band gap falls within one of the DDHF band gap values. This also demonstrates that for a given exchange value, every semiconducting system has a genuine band gap value, and the value of that exchange parameter can be determined using the self-consistent DDHF computation. Because the value of the exchange parameter is unknown, the inverse of the dielectric constant can be substituted for the exchange parameter value. The DDHF provide the ideal exchange value, which would otherwise be unknown.

D. DDHF calculations on bulk and monolayer doped systems

We began the hybrid functional computation with an initial guess of $\alpha = 25\%$. We measured the dielectric constant and band gap data once it reached self-consistency. In the next iteration, the mixing parameter is determined by $\alpha = \epsilon_\infty^{-1}$. This process is repeated until the dielectric constant and, as a result, the band gap converges. The convergence of the dielectric constant was checked with the k points and the number of bands. The converged band gap values calculated using DD-HSE06 and DD-PBE0 are tabulated in Table II and Table III for bulk and monolayer systems, respectively. On the other hand, in one run calculations, we have taken $\alpha = \frac{1}{\epsilon_\infty^{\text{PBE}}}$.

The symmetry of the system is slightly altered by the doping of the TM atom. In both the monolayer and bulk forms of the crystal, doping Ti, Cr, Mn, Ni, and Zn causes the system to transform into trigonal prismatic symmetry, with two sets of twofold degenerate orbitals and one nondegenerate orbital. These orbitals are named as e_1 ($d_{xy}/d_{x^2-y^2}$), e_2 (d_{yz}/d_{xz}). and a (d_{z^2}). The average values of the relaxed lattice parameters are $a = b = 3.64$ Å in monolayer, $a = b = 3.65$ Å and $c = 5.48$ Å in bulk systems with impurity doping. The average bond length of the transition metal atom and the S atom (d_{TM-S}) in transition metal doped monolayer and bulk systems are 2.42 Å and 2.40 Å, respectively. Whereas d_{TM-S} in monolayer and bulk pristine SnS_2 are 2.59 Å and 2.60 Å, respectively. The shorter bond length of the relaxed transition metal doped systems in comparison with the pristine system is due to the larger difference in the average electronegativity value between the transition metal atom and S atom (0.85) than the electronegativity difference between Sn atom and S atom (0.62). V, Cr, Mn, and Fe-doped bulk-SnS_2 systems are (nearly) direct-gap semiconductors that begin at the Γ point. Valence band edge is fixed at Γ point in all of these systems, such as the pristine bulk SnS_2. However, the conduction band edge has migrated from L (pristine SnS_2) to Γ point from pristine to all these doped systems. Because of the doping at the Sn site, conduction band has higher contribution from the d orbitals of the transition metal atom and less from the s orbital of the Sn atom in doped systems. The origin of the conduction band edge shifts from the s orbital of the Sn atom (pristine SnS_2) to the d orbital of the transition metal atom. As a result, 25% transition metal doping on SnS_2 crystal causes the switch from indirect to nearly direct gap semiconductor. As the atomic number of the transition metal increases among the semiconductors, the band gap decreases. We can see the highest band gap in Ti- and least in the Ni-doped systems. This is due to the shifting of the valence band towards the Fermi level. The valence band shifting enhances as the strength of the p-d hybridization increases. In all these doped systems, the nature of the conduction band changes as the atomic number of transition metal atoms increases, but the band structure at the valence band is almost the same.

TM-doped bulk SnS_2 systems: Our short-range hybrid functional computation estimates an upper bound to the band gap value of bulk SnS_2 as 2.35 eV and converges to 1.68 eV. According to various experimental studies, the band gap of bulk SnS_2 is found as 2.21–2.35 eV [21,92,96]. Even though our prediction of the band gap is 1.68–2.35 eV (Table II), the upper bound is matching with one of the experimental values. The experimental band gaps of TiS_2 and SnS_2 are found in the range of band gap values calculated using the DDHF. This ensures that the DDHF are good enough to produce the band gap range in which the experimental band gap exists. This

TABLE II. Band gap of bulk SnS_2 and TM-doped semiconductor systems estimated using DDHF calculations. Where $\alpha = \frac{1}{\epsilon^{SC-HSE}}$ and $\frac{1}{\epsilon^{SC-PBE0}}$ use converged dielectric constant calculated using HSE06 and PBE0 functionals under self-consistent scheme. $\alpha = \frac{1}{\epsilon^{\text{PBE}}}$ uses the dielectric constant calculated using PBE functional. Band gap values are in eV.

	HSE06			PBE0		
System	$\alpha = 25\%$	$\alpha = \frac{1}{\epsilon^{SC-HSE}}$	$\alpha = \frac{1}{\epsilon^{\text{PBE}}}$	$\alpha = 25\ \%$	$\alpha = \frac{1}{\epsilon^{SC-PBE0}}$	$\alpha = \frac{1}{\epsilon^{\text{PBE}}}$
Bulk-SnS_2	2.35	1.68	1.7	2.83	2.06	1.83
Ti	1.58	0.61	0.45	2.28	1.13	0.62
V	1.05	0.0	0.0	0.51	0.0	0.0
Mn	1.36	0.51	0.71	2.06	0.93	1.26
Fe	0.9	0	0.5	1.58	0.09	1.09
Ni	0.91	0.47	0.42	1.63	0.77	0.83

motivated us to perform DDHF calculations on other doped systems.

Both the HSE06 and PBE0 functionals revealed that Ti, V, Mn, Fe, and Ni-doped bulk SnS_2 systems are semiconductors with $\alpha = 25\%$. The band gap ranges estimated using short-range hybrid functionals for Ti, Mn, and Ni-doped systems are 0.61-1.58 eV, 0.51-1.36 eV and 0.47-0.91 eV, respectively, as shown in Table II, which has the band gap values corresponding to the initial guess of 25% exchange, converged with the dielectric constant and for the one-run calculation where $\alpha = \frac{1}{\epsilon^{\text{PBE}}}$. Apart from that, V and Fe-doped systems are semiconducting, with bandgaps of 1.05 eV and 0.9 eV as upper bounds, respectively. However, as we progressed through the self-consistent phases in the HSE06 calculations, V- and Fe-doped systems converged towards the half-metallic nature with a magnetic moment of 1 μ_B and 2 μ_B, respectively. PBE0 functionals shown in Table II produce slightly greater band gap values than HSE06 functionals. Still, the nature of the system remains the same except for Fe-doped SnS_2, which preserves its semiconducting nature with a very tiny gap of 0.09 eV. The band gap ranges calculated by the PBE0 functionals for Ti, V, Mn, Fe and Ni-doped bulk SnS_2 are 1.13–2.28 eV, 0.0–0.51 eV, 0.93–2.06 eV, 0.09–1.58 eV, and 0.77–1.63 eV, respectively.

Nonmagnetic semiconductors have converged in Ti- and Ni-doped systems. Ti-doped SnS_2 is synthesized experimentally [116] and found to be a semiconductor when the Ti concentration is below 30% [117]. Also, the GGA + U study predicts it as a semiconductor [118]. The semiconducting gap of 1.37 eV [119] and the GGA gap of 0.86 eV [119] in V-doped bulk SnS_2 were experimentally synthesized with 25% V concentration. When compared to the GGA gap, our HSE06 gap with 25% exchange gives an indirect band gap of 1.05 eV, which is a better value. Semiconducting V-doped SnS_2 thin films are made by spray pyrolysis [120] with a 25% V concentration. Under the DD-HSE06 and DD-PBE0 functionals, Cr-doping results in a half-metallic nature shown in bulk band structure Fig. 6(c). However, according to another DFT research, with low Cr content is a semiconductor [121]. Mn-doped SnS_2, converges out as a semiconductor with a magnetic moment of 3 μ_B. Under the HSE06 and PBE0 computations, Fe-doped SnS_2 is a semiconductor with 2 μ_B magnetic moment with 25% exchange. This is consistent with Fe-doped SnS_2 thin films produced experimentally [122]. Other DFT studies employing GGA + U [121,123,124] concur with the half-metal nature as we discovered in our inquiry after the system converges using DD-HSE06, which is shown in Table II. Aside from that, Fe-doped SnS_2 polycrystalline samples were produced via a molten salt solid-state process with Fe concentrations of 0, 12.5, 25, and 37.5% for impedance and dielectric analysis, according to Ref. [125]. Co-, Cu-, and Zn-doped systems are metals in the bulk environment regardless of the DFT functionals. For effective oxygen evolution reaction electrocatalyst, Co-doped SnS_2 nanosheet arrays were successfully produced experimentally [126]. The Zn-doped SnS_2 nanostructures were produced, and it was discovered as semiconductors with Zn concentrations below 10% [127]. Figures 6(a)–6(i) show the electronic band

TABLE III. Band gap of monolayer SnS_2 and TM-doped semiconductor systems estimated using DDHF calculations. Where, $\alpha = \frac{1}{\epsilon^{SC-HSE}}$ and $\frac{1}{\epsilon^{SC-PBE0}}$ use converged dielectric constant calculated using HSE06 and PBE0 functionals under self-consistent scheme. $\alpha = \frac{1}{\epsilon^{\text{PBE}}}$ uses the dielectric constant calculated using PBE functional. Band gap values are in eV.

	HSE06			PBE0		
System	$\alpha = 25\%$	$\alpha = \frac{1}{\epsilon^{SC-HSE}}$	$\alpha = \frac{1}{\epsilon^{\text{PBE}}}$	$\alpha = 25\ \%$	$\alpha = \frac{1}{\epsilon^{SC-PBE0}}$	$\alpha = \frac{1}{\epsilon^{\text{PBE}}}$
ML-SnS_2	2.43	1.89	1.85	3.11	2.23	2.11
Ti	1.80	1.17	1.05	2.48	1.60	1.25
V	1.30	0.0	0.0	1.75	0.0	0.0
Cr	1.72	0.0	0.0	2.44	0.54	0.3
Mn	1.75	1.03	0.93	2.43	1.34	1.1
Fe	1.50	0.31	0.02	2.19	0.63	0.05
Ni	1.50	0.99	0.94	2.22	1.27	1.11
Cu	0.0	0.0	0.0	0.73	0.0	0.0

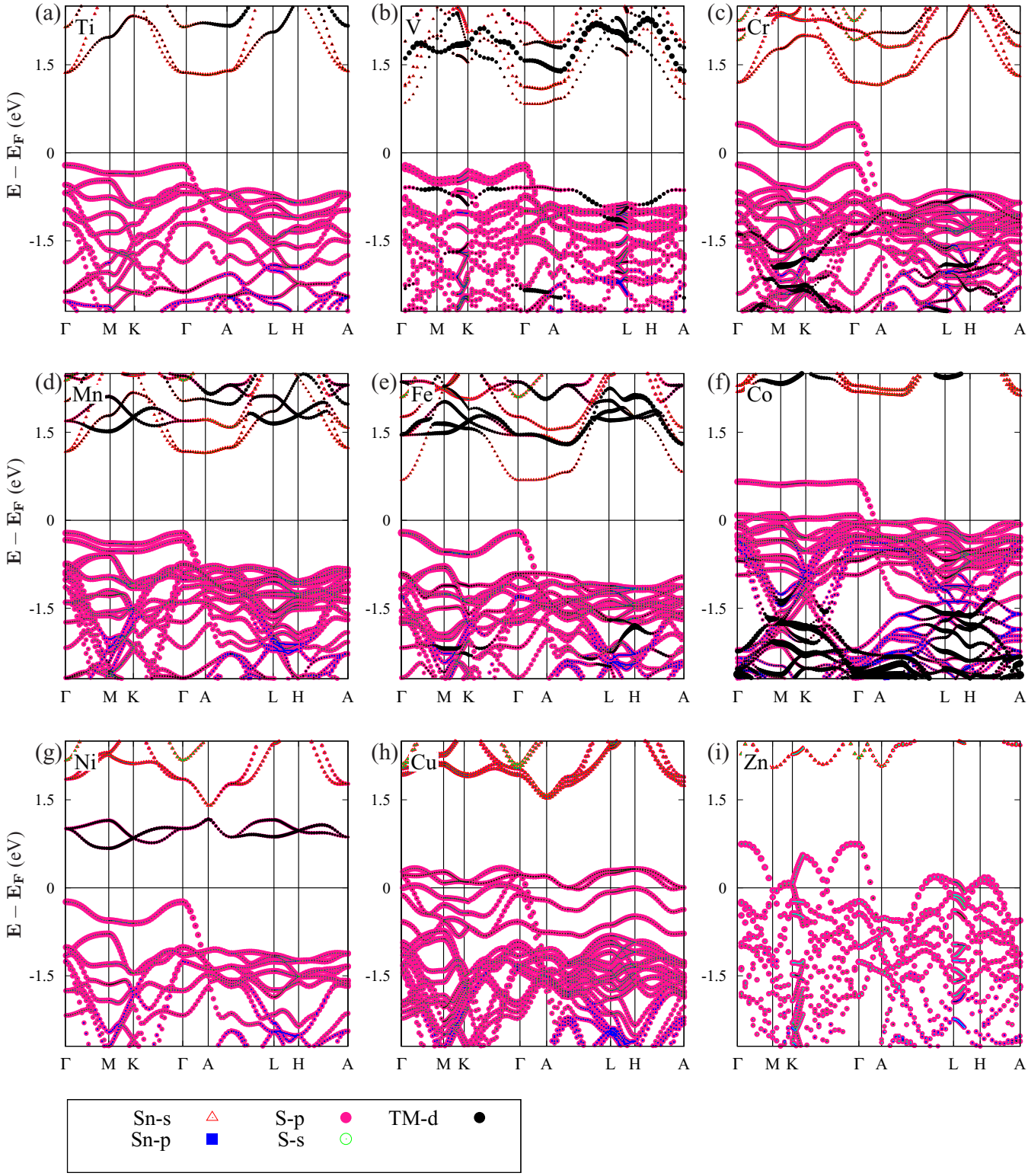

FIG. 6. Orbital projected band structure of (a) Ti, (b) V, (c) Cr, (d) Mn, (e) Fe, (f) Co, (g) Ni, (h) Cu, and (i) Zn-doped bulk SnS_2 calculated using HSE06 functionals with an exchange of 25%. Fermi energy is set to zero.

structure of Ti- to Zn-doped bulk SnS_2 systems using HSE06 functionals with 25% exchange.

TM-doped monolayer SnS_2 system: The experimental band gap of monolayer SnS_2 is 2.29 eV [97]. This is in the range of 1.89–2.43 eV calculated by DD-HSE06 and 2.23–3.11 eV by DD-PBE0 (Table III), which is in good agreement with the various theory works (Table I). Our PBE0 functionals with an exchange of 11.6% gives a band gap of 2.24 eV (Supplemental Material [86], Table IX), which is in good agreement with the experimental value. Also the HSE06 functionals with an exchange of 13.9% estimates a band gap of 1.95 eV (Supplemental Material [86], Table VIII). As per the dielectric-dependent HSE06 functionals Ti (1.17–1.8 eV, 0 μ_B), Mn (1.03–1.75 eV, 3 μ_B), Fe (0.31–1.50 eV, 2 μ_B), and Ni (0.99–1.50 eV, 0 μ_B)-doped monolayer SnS_2 are semiconductors. V (0.0–1.3 eV, 1 μ_B) and Cr (0.0–1.72 eV, 2 μ_B)-doped systems are semiconductors at the initial guess, and converged to half-metals. These band gap values are listed in the Table III. The PBE0 functionals reveal that Cr (0.54–2.44 eV, 2 μ_B)-doped system converges to semiconductor and Cu

(0.73 eV, 0 μ_B)-doped system initially has a semiconducting nature and converges to half-metal. Regardless of the DFT functionals used, Ti- and Ni-doped systems converged into nonmagnetic semiconductors in the bulk and monolayer phases. The same is stated in another DFT study [128]. Even though the V-doped system has a semiconductor nature with $\alpha = 25\%$, the DD-HSE06 and DD-PBE0 computations converge to a half-metallic nature (Supplemental Material [86], Tables VIII and IX). At 6.25% V concentration, a DFT study revealed that the V-doped SnS_2 monolayer is a semiconductor [128]. In a monolayer environment, a Cr-doped system is a semiconductor with $\alpha = 25\%$, while it is half-metal in the bulk environment. Experimentally produced Cr-doped SnS_2 nanoflowers were found to be semiconductors [129]. Mn- and Fe-doped systems converged during the monolayer phase to form magnetic semiconductors. Single crystals of Mn-doped SnS_2, which are semiconductors, were produced experimentally using the self-flux method [130]. The Fe-doped SnS_2 monolayer produced experimentally is a magnetic semiconductor [131]. Through strain engineering, the DFT investigation of Fe-doped monolayer SnS_2 is a half-metal [132] and Mn-doped monolayer SnS_2 is a semiconductor [133]. We discovered metallic nature in the Co and Zn-doped environment. The intercalated Co-SnS_2 and Cu-SnS_2 monolayers are metal and p-type semiconductors, respectively, according to the experiment [134]. When DD-PBE0 functionals are utilized with $\alpha = 25\%$ exchange, the Cu-doped system is found to be a semiconductor with a finite gap of 0.73 eV. Once the convergence is achieved, the system approaches half-metallic nature. Throughout the DD-HSE06 computation, it is a half-metal. Cu-doped SnS_2 nanoflakes were made using a hydrothermal technique, according to Ref. [135]. Zn-doped SnS_2 nanoflakes were synthesized and showed that the system turns semiconductor at very low Zn concentrations [136]. At low Zn concentrations, the DFT work on the Zn-doped SnS_2 monolayer also indicates it to be a semiconductor [83]. Figures 7(a)–7(i) show the electronic band structure of Ti- to Zn-doped monolayer SnS_2 systems using HSE06 functionals with 25% exchange.

IV. OPTICAL PROPERTIES

The study of the optical properties of a photovoltaic absorber is important for building optoelectronic devices. Due to impurity, transition metal doped systems have a smaller band gap than pure SnS_2 (2.2–2.43 eV). According to the HSE06 band structure calculation with 25% exchange, the band gap of bulk and monolayer doped systems vary within 0.9–1.58 eV and 1.5–1.8 eV, respectively. In these systems, V-, Mn-, and Fe-doped systems are nearly direct gap semiconductors in the bulk form. This is shown in the Figures 6(b), 6(d), and 6(e). The optical properties we focus on are the absorption coefficient $\alpha(\omega)$, reflectivity $R(\omega)$, refractive index $n(\omega)$, and exciton binding energy. For the study, we use HSE06 functionals with 25% exchange. Optical constants have a dependence on the dielectric function $\varepsilon(\omega)$, which has a dependence on the frequency of the incident photon. To completely understand the optical properties, we need to calculate its dielectric function $\varepsilon(\omega)$. The complex dielectric function is given by

$$\varepsilon(\omega) = \varepsilon_1(\omega) + i\varepsilon_2(\omega). \tag{24}$$

Here $\varepsilon_1(\omega)$ is the real and $\varepsilon_2(\omega)$ is the imaginary part of the dielectric function. The real part of the dielectric function is obtained by the Kramers-Kronig transformation [83]. It is given by

$$\varepsilon_1(\omega) = \frac{2}{\pi} P \int_0^\infty \frac{\omega' \varepsilon_2(\omega') d\omega}{(\omega'^2 - \omega^2)}. \tag{25}$$

Where P denotes the principle value. The imaginary part of the dielectric function is determined by summation over empty states using the equation [137]

$$\varepsilon_2(\omega) = \left(\frac{4\pi^2 e^2}{m^2\omega^2}\right) \sum_{i,j} \int \langle i|M|j\rangle^2 f_i(1 - f_i) \times (E_f - E_i - \omega) d^3k. \tag{26}$$

Here M is the dipole matrix, i and j are the initial and final states respectively, f_i is the Fermi distribution function for the ith state, and E_i is the energy of electron in the ith state. The optical constants such as absorption coefficient $\alpha(\omega)$, reflectivity $R(\omega)$, and refractive index $n(\omega)$ can be calculated by the real $\varepsilon_1(\omega)$ and imaginary $\varepsilon_2(\omega)$ part of the dielectric functions [138–140]. They are given by

$$\alpha(\omega) = \sqrt{2}\omega\left[\sqrt{\varepsilon_1^2(\omega) + \varepsilon_2^2(\omega)} - \varepsilon_1(\omega)\right]^{1/2}, \tag{27}$$

$$n(\omega) = \frac{1}{\sqrt{2}}\left[\sqrt{\varepsilon_1^2(\omega) + \varepsilon_2^2(\omega)} + \varepsilon_1(\omega)\right]^{1/2}, \tag{28}$$

$$\kappa(\omega) = \frac{1}{\sqrt{2}}\left[\sqrt{\varepsilon_1^2(\omega) + \varepsilon_2^2(\omega)} - \varepsilon_1(\omega)\right]^{1/2}. \tag{29}$$

Here $\kappa(\omega)$ is the extinction coefficient, which gives reflectivity as

$$R(\omega) = \frac{(n-1)^2 + \kappa^2}{(n+1)^2 + \kappa^2}. \tag{30}$$

Bulk-SnS_2 crystal has an absorption peak at 3.35 eV with an absorption coefficient of $2.2 \times 10^4 \text{cm}^{-1}$. In comparison to the monolayer SnS_2, the bulk absorption spectra have shifted to the low-energy region. This might be due to the presence of

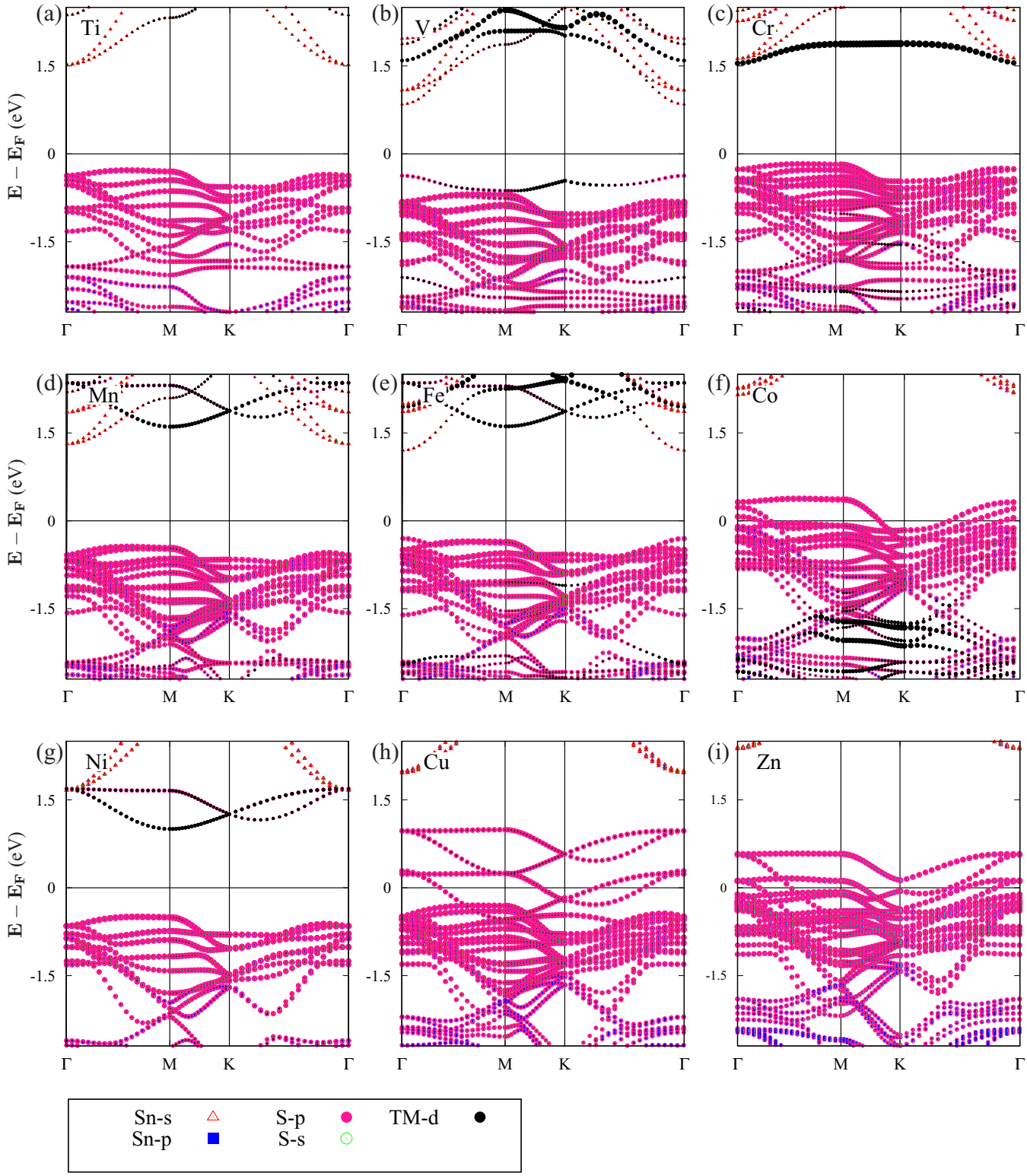

FIG. 7. Orbital projected band structure of (a) Ti, (b) V, (c) Cr, (d) Mn, (e) Fe, (f) Co, (g) Ni, (h) Cu, and (i) Zn-doped monolayer SnS_2 calculated using HSE06 functionals with an exchange of 25%. Fermi energy is set to zero.

several layers in the bulk system, which are stacked by van der Waals interaction. The electrons in these layers undergo an interband transition from valence band maxima near Γ point to conduction band minima at *L* point. The indirect band gap calculated using absorption spectra is 2.22 eV. For pure SnS_2, the first prominent peak in the entire energy region is located at 6.3 eV, and two small peaks are positioned at 3.35 eV and 4.36 eV. The higher-intensity peaks are observed

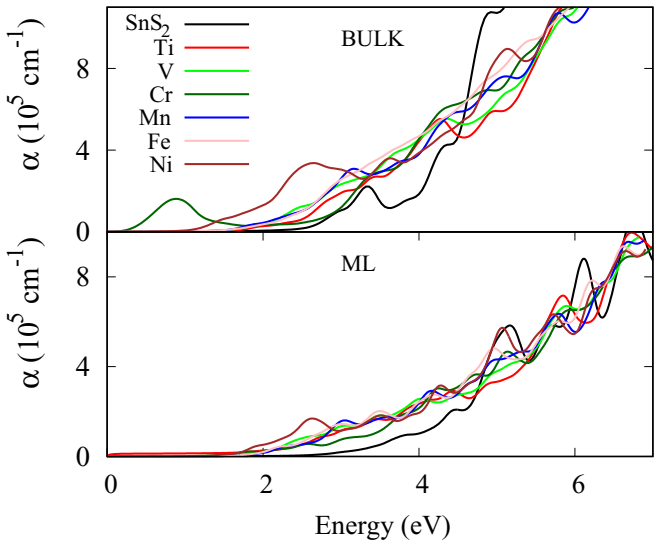

FIG. 8. Optical absorption spectra of pristine SnS_2 and TM-doped bulk and monolayer SnS_2 systems for semiconductors.

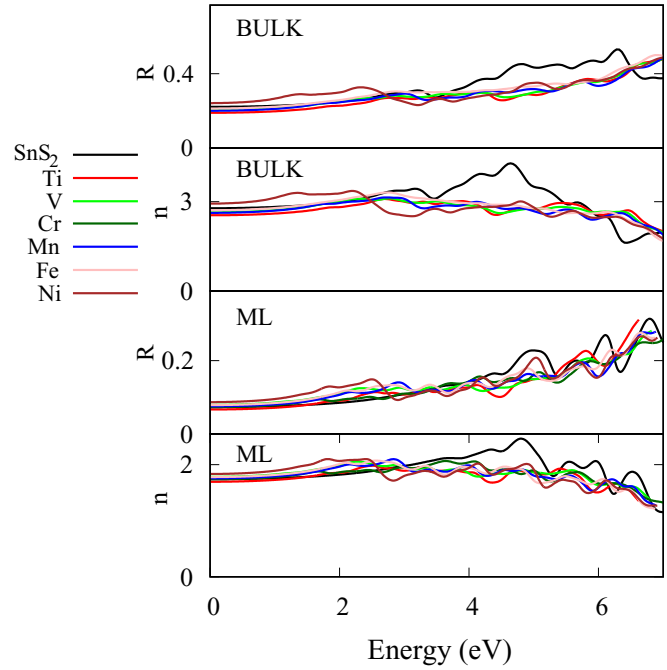

FIG. 9. Reflectivity and refractivity spectra of pristine SnS_2 and TM-doped bulk and monolayer SnS_2 systems for semiconductors.

above 6.3 eV. This shows that more of the absorption occurs in the near-ultraviolet region. The absorption spectra of all the doped systems are shown in Fig. 8 in comparison with the pristine SnS_2. This shows the red shift in the energy of all the transition metal doped systems in comparison with the pristine SnS_2. This red shift is due to the mediation of impurity $3d$ bands of the transition metal atoms near the Fermi level of the system. This can also be verified from the band structure calculations. In comparison with pure SnS_2, the absorption coefficient of the doped system has increased. Ni-doped system has the highest absorption in the lower-energy range than the other doped systems. The behavior of the Cr-doped system is different from other systems. It resembles free-electron absorption. This is because of the half-metallic nature of the Cr-doped system in the bulk form. However Cr-doped system in monolayer form is a semiconductor. It undergoes a transition from a bulk half-metallic system to a monolayer semiconductor when it is doped at 25% concentration. Co-, Cu-, and Zn-doped systems also have metallic absorption. The metallic nature can be seen from the absorption at zero energy in Supplemental Material [86], Fig. 11. All the transition metal doped systems look similar in the (near) infrared region. From the absorption spectra with 25% dopant concentration, we can see the enhanced absorption coefficient. This shows that these systems have a higher tendency of light absorption in the near-ultraviolet region. Supplemental Material [86], Fig. 11 shows the optical absorption in Co-, Cu-, and Zn-doped SnS_2 systems. We can also see how the concentration of dopant affects the absorption by using the example of the Fe-doped monolayer SnS_2. As the concentration of Fe in the SnS_2 crystal increases, the absorption peaks shift towards the low-energy region. In other words, the band gap becomes narrower as the Fe concentration increases (Supplemental Material [86], Fig. 11).

The reflectivity (R) and refractivity index (n) spectra of SnS_2 and all the doped systems are presented in Fig. 9. Both the spectra of the doped systems are enhanced below 3 eV energy which is highest in Ni-doped SnS_2 in comparison with the pure SnS_2 crystal. Above 3 eV, reflectivity and refractivity of the doped systems are less enhanced in comparison with the pure SnS_2. We have seen the significant absorption of all these doped systems below 3 eV. Hence all these results together indicate that the optical properties are greatly improved in the low-energy region.

Exciton binding energy

Excitons are the bound state of electrons and holes. Excitons play a vital role in the optical properties of the crystal. The behavior of the excitons in a system purely depends on the electronic environment of the system. The bulk system is surrounded by a dielectric medium thoroughly from all three directions, and hence the Coulomb interaction between electron and hole is well screened by the dielectric medium. In the case of a 2D system, the screening effect is reduced and is confined only to the 2D plane. On top of this, quantum confinement also adds to the dielectric confinement in the 2D system. Finally, these two confinement effects make the exciton to be tightly bound on 2D plane rather than in the bulk environment of the system. This fact leads to higher binding energy in monolayer systems. Hence it is very important to understand the dielectric screening in 2D semiconductors or insulators. The dielectric screening can be measured using the screening length r_0. For a better understanding we adopted the theory described by other work [141], we imagine a 2D dielectric sheet embedded in a vacuum exposed to an external potential caused by a point charge placed at the origin. In the long-wavelength limit, the induced charge density is related to the 2D polarization P_{2D}. Then using Poisson's equation, the total electrostatic potential generated by the point charge can

be given by [141],

$$\nabla^2\phi(\mathbf{r}) = -4\pi e\delta(\mathbf{r}) - 4\pi\chi_{2D}\nabla^2\phi(\rho, z=0)\delta(z). \quad (31)$$

Then by using the Fourier transform, we can get the 2D macroscopic potential.

$$\phi_{2D}(\mathbf{q}) = \frac{2\pi e}{|q|(1+2\pi\chi_{2D}|q|)}. \quad (32)$$

Here q is the in-plane component of the wave vector, and the χ_{2D} is the 2D polarizability of the dielectric sheet. Here ϕ_{2D} describes the 2D macroscopic screening of a point charge. By considering the above expression of ϕ_{2D}, it is evident that the macroscopic dielectric screening has no connection with a simple dielectric constant, whereas that plays a role in 3D systems. Now by the inverse Fourier transform of the $e\phi_{2D}(q)$, one can determine the effective potential experienced by the electron in a dielectric 2D plane in the presence of a point charge. This was originally derived by Keldysh [142]

$$V_{2D}(\mathbf{r}) = -\frac{e^2}{8\varepsilon_0\bar{\varepsilon}r_0}\left[H_0\left(\frac{r}{r_0}\right) - Y_0\left(\frac{r}{r_0}\right)\right]. \quad (33)$$

Where H_0 and Y_0 are the Struve and the second kind of Bessel functions, respectively. We have $r_0 = 2\pi\chi_{2D}/\kappa_{\text{eff}}$, where κ_{eff} is the effective dielectric constant of the environment surrounding the 2D system. With χ_{2D} calculated using the relation $\varepsilon_{xy} = 1 + 4\pi\chi_{2D}/L$. Here ε_{xy} is the in-plane dielectric constant, and L is the thickness of the vacuum layer. From the expression of the 2D effective potential created by a point charge, we can understand that this potential depends on distance r, relative to r_0. The simplified potential given by Keldysh [142] when $r \ll r_0$ is

$$V_{2D}(r \ll r_0) \approx \frac{e^2}{4\pi\varepsilon_0\bar{\varepsilon}}\frac{1}{r_0}\left[ln\left(\frac{r}{2r_0}\right) + \gamma\right]. \quad (34)$$

Here γ is the Euler constant. When $r \gg r_0$,

$$V_{2D}(r \gg r_0) \approx -\frac{e^2}{4\varepsilon_0\bar{\varepsilon}}\frac{1}{r}. \quad (35)$$

One can notice the logarithmic potential like a line charge in the case of $r \ll r_0$ and in the case of $r \gg r_0$ the potential varies like $\frac{1}{r}$, which is a standard electrostatic potential created by a point charge [143]. The combination of these two limits is expressed in a single equation by Cudazzo *et al.* [141], given by

$$V_{2D}^{C}(r \ll r_0) \approx \frac{e^2}{4\pi\varepsilon_0\bar{\varepsilon}}\frac{1}{r_0}\left[ln\left(\frac{r}{r+r_0}\right) + [\gamma - ln(2)]e^{-\frac{r}{r_0}}\right]. \quad (36)$$

For a 2D system with anisotropic electron and hole, effective masses $m_x{}^e \neq m_y{}^e$, and $m_x{}^h \neq m_y{}^h$, the exciton wave function obtained using variational principle is given by [144]

$$\phi(x,y) = \left(\frac{2}{a_x^2\lambda\pi}\right)^{1/2}\exp[-\sqrt{(x/a_x)^2 + (y/\lambda a_x)^2}]. \quad (37)$$

Here λ is the variational anisotropy scaling factor, a_x is the exciton extension along the x direction, λ and a_x are related by $a_y = \lambda a_x$. Using this variational wave function, the kinetic and potential energies of exciton are given by [143]. The expression for the kinetic energy is

$$E_{\text{kin}}(a_x,\lambda) = \frac{\hbar^2}{2}\iint\phi\left[\frac{1}{\mu_x}\frac{\partial^2\phi}{\partial x^2} + \frac{1}{\mu_y}\frac{\partial^2\phi}{\partial y^2}\right]dxdy, \quad (38)$$

$$E_{\text{kin}}(a_x,\lambda) = \frac{\hbar^2}{4a_x^2}\left(\frac{1}{\mu_x} + \frac{1}{\lambda^2\mu_y}\right). \quad (39)$$

Here μ_x and μ_y are the reduced effective masses of the exciton along x and y directions respectively, $\mu = m^e m^h/(m^e + m^h)$. The potential energy is given by

$$E_{\text{pot}}(a_x,\lambda) = \iint V_{2D}(x,y)\phi(x,y)^2 dxdy. \quad (40)$$

Using the expected kinetic and potential energy of the exciton, its binding energy is expressed as

$$E_{X-2D}(a_x,\lambda) = E_{\text{kin}} + E_{\text{pot}}. \quad (41)$$

Where E_{X-2D} specifies the exciton binding energy in a 2D system, the detailed study of the exciton binding energy mentioned in Ref. [145] leads to running a *Mathematica* code to calculate E_{X-2D}. Using the above expression (41) formulated by the *Mathematica* code of version 10.2.0 [146], we calculated the exciton binding energy of all the monolayer systems doped with TM atoms. This requires the effective masses of the charge carriers along x, y directions and the 2D polarizability χ_{2D}. The effective masses of charge carriers are calculated by fitting the HSE06 bands to the parabolic dispersion $E(k) = \frac{\hbar^2k^2}{2m^*}$ using VASPKIT version 0.52 [147].

TABLE IV. Effective masses of electron $m_e^*(k_x)$, $m_e^*(k_y)$, $m_e^*(k_z)$ and hole $m_h^*(k_x)$, $m_h^*(k_y)$, $m_h^*(k_z)$ along x, y, z directions for the bulk-SnS_2 and doped semiconductor systems. Also the reduced 3D effective mass, $\mu^{3D} = 3(\mu_x^{-}1 + \mu_y^{-}1 + \mu_z^{-}1)^{-1}$, the effective bulk dielectric constant κ_B, and the exciton binding energy E_{X-3D} values are given. Here $\mu_i = (m_i^e m_i^h)/(m_i^e + m_i^h)$. Effective masses are in units of the electron rest mass.

	System	$m_e^*(k_x)$	$m_e^*(k_y)$	$m_e^*(k_z)$	$m_h^*(k_x)$	$m_h^*(k_y)$	$m_h^*(k_z)$	μ_{3D}	κ_B	$E_{X-3D}(meV)$	
BULK-SnS_2	[90]	1.104	0.375		0.424	2.542		0.345	5.85	137	112 (expt) [90]
	Present work	1.095	0.398	1.221	0.422	2.460	2.10	0.398	6.56	126.2	
	Ti	0.476	0.419	1.14	3.269	3.269	0.239	0.295	5.79	120.3	
	V	0.314	0.325	4.032	0.458	0.337	1.043	0.238	6.19	84.72	
	Mn	0.909	0.612	3.194	1.355	7.38	2.405	0.394	5.77	161.3	
	Fe	3.142	0.508	0.304	0.792	0.496	7.263	0.375	6.68	114.9	
	Ni	0.64	1.024	4.464	2.13	1.795	0.239	0.376	8.09	78.31	

TABLE V. Effective masses of electron $m_e^*(k_x)$, $m_e^*(k_y)$ and hole $m_h^*(k_x)$, $m_h^*(k_y)$ along x and y directions for the monolayer-SnS_2 and doped semiconductor systems. Also the reduced 2D polarizability χ_{2D} and the exciton binding energy E_{X-2D} values are given. Effective masses are in units of the electron rest mass.

	System	$m_e^*(k_x)$	$m_e^*(k_y)$	$m_h^*(k_x)$	$m_h^*(k_y)$	χ_{2D}(Å)	$E_{X-2D}(eV)$
ML-SnS_2	[90]	0.342	0.815		0.342	2.266	0.912
	Present work	0.340	0.810	0.335	2.272	2.28	0.926
	Ti	0.869	0.663	0.60	0.436	2.11	1.293
	V	0.658	0.346	2.486	0.112	2.03	1.055
	Cr	0.638	0.682	2.609	0.407	1.88	1.46
	Mn	0.526	0.657	1.988	0.450	2.04	1.42
	Fe	0.277	0.483	0.426	2.134	2.18	1.24
	Ni	0.740	0.895	2.127	0.384	2.3	1.295

Let us consider the excitons in a 3D system. The dielectric screening is neglected while formulating the exciton binding energy in a 3D system. By using the effective mass theory of excitons developed by Velizhanin *et al.* [148] the 2D exciton binding energy is approximated to the 3D systems [90]. The exciton binding energy in the 3D system is given by [90]

$$E_{X-3D} = \frac{\mu^{3D} E_{\mathrm{Ryd}}}{\kappa_B^2} \tag{42}$$

Here $\mu^{3D} = 3(\mu_x^{-}1 + \mu_y^{-}1 + \mu_z^{-}1)^{-1}$, $\mu_i = (m_i^e m_i^h)/(m_i^e + m_i^h)$, and κ_B is the effective bulk dielectric constant calculated using the bulk dielectric tensor. The expression is given by $\kappa_B = \sqrt{\varepsilon_z \varepsilon_{xy}}$, with ε_z and ε_{xy} are the transverse and in-plane component of the bulk dielectric tensor.

We computed the dielectric tensor by using HSE06 functionals. Using the above formula (42), we calculated the exciton binding energy of the bulk SnS_2 crystal as 126.2 meV, which is near to the calculated value by other theory work [90] (137 meV). Also, it is in good agreement with the experimental work [149] (112 meV). Tables IV and V provide the exciton binding energy of all the bulk and monolayer doped SnS_2 systems along with the required parameters. The calculated value of E_{X-2D} for the pristine monolayer SnS_2 is 0.926 eV, which is in good agreement with the other theory value [90] (0.912 eV). The variation in the exciton binding energy after doping with the transition metal atoms is mainly due to the involvement of the localized 3d orbitals, which are absent in the pristine system. These 3d orbitals change the hybridization between the host and chalcogen atom. Thus changing the extrema positions. This affects the curvature of the electron path in the valence and conduction band. Since the curvature of the electron has an inverse dependence on its effective mass, exciton binding energy changes accordingly. The plot in Fig. 10 shows that, in the case of bulk doped systems Mn-doped system has the highest exciton binding energy of 161 meV. To our knowledge, this large exciton binding energy is because of the higher reduced effective exciton mass due to the flat band near the Fermi level. This can be seen in the Mn-band structure in Fig. 6(d). This flat valence band is due to the p_z orbital of S and d_z^2 orbital of Mn atom. Also note that it has a lower value of bulk dielectric constant (5.77) than other systems. Further, the flatness of this band is more towards Γ to M path, and hence the hole mass is heavier (7.38 m_0) along the x direction. The electron mass in the conduction band is lighter than the hole mass, as shown in the band structure in Fig. 6(d), which has more curvature than the flat valence band. Second, Ti- and Fe-doped systems also have larger binding energies of 120.3 meV and 114.9 meV, respectively. In this case, it is mainly because of the effective mass of the carriers.

In the Fe-doped system, the spin-up hole has heavier mass along the y direction due to a flat curve along Γ to M path. This valence band just below the Fermi level is mainly due to p_z orbital of S atom and d orbitals of Fe atom. The same trend holds for the Ti-doped system. The valence band is flatter than that of the Fe-doped system. In the conduction band, the path along Γ to A has heavier electron because the corresponding band has more contribution from the localized $d_{xy}/d_{x^2-y^2}$ and d_{xz}/d_{yz} orbitals of Ti atom with very less s-orbital contribution from Sn atom. This implies a heavier electron along the z direction. These observations can be seen in Ti- and Fe-doped systems' band structure in Figs. 6(a) and 6(e). In the case of V- and Ni-doped systems, the charge carriers possess lighter effective masses along x, and y directions, though the electron has a heavier mass along the z direction. Their bulk dielectric constants are higher compared to other systems. These two factors compensate and result in smaller exciton binding energy in Ti- and V-doped systems. Figure 10 shows the comparison between the exciton binding energy of all of the transition metal doped semiconducting systems in bulk and monolayer environment. Among these systems, exciton

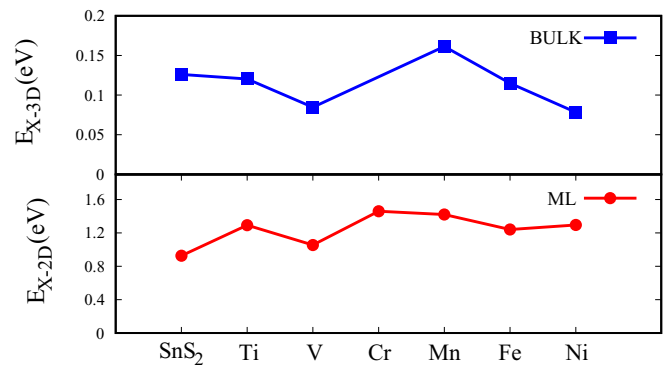

FIG. 10. Exciton binding energy in TM-doped monolayer and bulk SnS_2 systems.

binding energy is larger in the monolayer than in the bulk environment.

V. CONCLUSION

In conclusion, we have systematically studied the electronic band gap and optical properties of all the 3*d*-series transition metal doped SnS_2 crystal both in the bulk and monolayer form. Calculation of the formation energies shows that the Sn-poor (S-rich) condition is the favorable condition to incorporate the TM atom into SnS_2 crystal at Sn site. The dielectric-dependent hybrid functionals calculations have predicted the experimentally matchable band gaps for TiS_2 and SnS_2 crystals. Using the dielectric-dependent HSE06 and PBE0 hybrid functionals, we have calculated the range of band gap values for all the doped systems in bulk and monolayer environment. The converged band gap is calculated at the level of the converged dielectric constant. The calculated range of band gap values using DDHF give the lower and upper bound to the true band gap of the system. Possible experimental gaps are expected within this range. This helps us to determine the application perspectives of the transition metal doped systems.

The absorption spectra reveal the red shift in the energy of all the doped systems. V-, Mn-, and Fe-doped systems are nearly direct band gap semiconductors and exhibit higher absorption coefficients in the bulk environment. These are suitable optical absorber materials for optoelectronic devices. Cr doped bulk SnS_2 is a half-metal that is good for spin-injector materials. The absorption coefficient, reflectivity and refractivity of all the doped systems are enhanced in the low-energy region. Thus, our calculations support the effective use of solar energy. Semiconductors with a monolayer environment show higher exciton binding energy than in the bulk environment. These results emphasize the importance of transition metal doping on SnS_2 crystal for optoelectronic device applications.

ACKNOWLEDGMENTS

The author acknowledges Dr. Mukul Kabir and the Department of Physics, Indian Institute of Science Education and Research, Pune.

[1] K. S. Novoselov, A. K. Geim, S. V. Morozov, D. Jiang, Y. Zhang, S. V. Dubonos, I. V. Grigorieva, and A. A. Firsov, Science **306**, 666 (2004).
[2] H. Kasai, K. Tolborg, M. Sist, J. Zhang, V. R. Hathwar, M. Ø. Filsø, S. Cenedese, K. Sugimoto, J. Overgaard, E. Nishibori, and B. B. Iversen, Nature Mater. **17**, 249 (2018).
[3] P. Chen, W. W. Pai, Y.-H. Chan, A. Takayama, C.-Z. Xu, A. Karn, S. Hasegawa, M. Y. Chou, S.-K. Mo, A.-V. Fedorov, and T.-C. Chiang, Nature Commun. **8**, 516 (2017).
[4] M. N. Gjerding, R. Petersen, T. G. Pedersen, N. A. Mortensen, and K. S. Thygesen, Nature Commun. **8**, 320 (2017).
[5] L. Yu, Q. Yan, and A. Ruzsinszky, Nature Commun. **8**, 15224 (2017).
[6] W. Zhang, Z. Huang, W. Zhang, and Y. Li, Nano Res. **7**, 1731 (2014).
[7] M. Chhowalla, H. S. Shin, G. Eda, L.-J. Li, K. P. Loh, and H. Zhang, Nature Chem. **5**, 263 (2013).
[8] Y. I. Joe, X. M. Chen, P. Ghaemi, K. D. Finkelstein, G. A. de la Peña, Y. Gan, J. C. T. Lee, S. Yuan, J. Geck, G. J. MacDougall, T. C. Chiang, S. L. Cooper, E. Fradkin, and P. Abbamonte, Nature Phys. **10**, 421 (2014).
[9] K. Xu, Z. Wang, F. Wang, Y. Huang, F. Wang, L. Yin, C. Jiang, and J. He, Adv. Mater. **27**, 7881 (2015).
[10] S. Mathias, S. Eich, J. Urbancic, S. Michael, A. V. Carr, S. Emmerich, A. Stange, T. Popmintchev, T. Rohwer, M. Wiesenmayer, A. Ruffing, S. Jakobs, S. Hellmann, P. Matyba, C. Chen, L. Kipp, M. Bauer, H. C. Kapteyn, H. C. Schneider, K. Rossnagel *et al.*, Nature Commun. **7**, 12902 (2016).
[11] Q. Zhao, Y. Guo, K. Si, Z. Ren, J. Bai, and X. Xu, physica status solidi (b) **254**, 1700033 (2017).
[12] R. Prins, V. H. J. D. Beer, and G. A. Somorjai, Catal. Rev. **31**, 1 (1989).
[13] M. Salmeron, G. Somorjai, A. Wold, R. Chianelli, and K. Liang, Chem. Phys. Lett. **90**, 105 (1982).
[14] T. F. Jaramillo, K. P. Jørgensen, J. Bonde, J. H. Nielsen, S. Horch, and I. Chorkendorff, Science **317**, 100 (2007).
[15] S. M. Ahmed and H. Gerischer, Electrochim. Acta **24**, 705 (1979).
[16] H. Fang, S. Chuang, T. C. Chang, K. Takei, T. Takahashi, and A. Javey, Nano Lett. **12**, 3788 (2012).
[17] W. Zhao, Z. Ghorannevis, L. Chu, M. Toh, C. Kloc, P.-H. Tan, and G. Eda, ACS Nano **7**, 791 (2013).
[18] K.-K. Liu, W. Zhang, Y.-H. Lee, Y.-C. Lin, M.-T. Chang, C.-Y. Su, C.-S. Chang, H. Li, Y. Shi, H. Zhang, C.-S. Lai, and L.-J. Li, Nano Lett. **12**, 1538 (2012).
[19] G. L. Frey, R. Tenne, M. J. Matthews, M. S. Dresselhaus, and G. Dresselhaus, J. Mater. Res. **13**, 2412 (1998).
[20] A. R. Beal, H. P. Hughes, and W. Y. Liang, J. Phys. C **8**, 4236 (1975).
[21] D. Greenaway and R. Nitsche, J. Phys. Chem. Solids **26**, 1445 (1965).
[22] L. A. Burton, T. J. Whittles, D. Hesp, W. M. Linhart, J. M. Skelton, B. Hou, R. F. Webster, G. O'Dowd, C. Reece, D. Cherns, D. J. Fermin, T. D. Veal, V. R. Dhanak, and A. Walsh, J. Mater. Chem. A **4**, 1312 (2016).
[23] T.-J. Kim, C. Kim, D. Son, M. Choi, and B. Park, J. Power Sources **167**, 529 (2007).
[24] J.-w. Seo, J.-t. Jang, S.-w. Park, C. Kim, B. Park, and J. Cheon, Adv. Mater. **20**, 4269 (2008).
[25] W. Shi, L. Huo, H. Wang, H. Zhang, J. Yang, and P. Wei, Nanotech. **17**, 2918 (2006).
[26] H. Zhong, G. Yang, H. Song, Q. Liao, H. Cui, P. Shen, and C.-X. Wang, J. Phys. Chem. C **116**, 9319 (2012).
[27] D. De, J. Manongdo, S. See, V. Zhang, A. Guloy, and H. Peng, Nanotech. **24**, 025202 (2013).
[28] H. S. Song, S. L. Li, L. Gao, Y. Xu, K. Ueno, J. Tang, Y. B. Cheng, and K. Tsukagoshi, Nanoscale **5**, 9666 (2013).

[29] A. Sanchez-Juarez and A. O. z, Semicond. Sci. Technol. **17**, 931 (2002).

[30] A. A. Ahmad, A. Migdadi, A. M. Alsaad, I. Qattan, Q. M. Al-Bataineh, and A. Telfah, Heliyon **8**, e08683 (2022).

[31] S. Rühle, Solar Energy **130**, 139 (2016).

[32] W. Shockley and H. J. Queisser, J. Appl. Phys. **32**, 510 (1961).

[33] P. Yang, L.-J. Shi, J.-M. Zhang, G.-B. Liu, S. A. Yang, W. Guo, and Y. Yao, J. Phys. D **51**, 025105 (2018).

[34] M. M. Khan, S. A. Ansari, D. Pradhan, M. O. Ansari, D. H. Han, J. Lee, and M. H. Cho, J. Mater. Chem. A **2**, 637 (2014).

[35] J. Nowotny, M. A. Alim, T. Bak, M. A. Idris, M. Ionescu, K. Prince, M. Z. Sahdan, K. Sopian, M. A. Mat Teridi, and W. Sigmund, Chem. Soc. Rev. **44**, 8424 (2015).

[36] S. Kalathil, M. M. Khan, S. A. Ansari, J. Lee, and M. H. Cho, Nanoscale **5**, 6323 (2013).

[37] A. Chaves, J. G. Azadani, H. Alsalman, D. R. da Costa, R. Frisenda, A. J. Chaves, S. H. Song, Y. D. Kim, D. He, J. Zhou, A. Castellanos-Gomez, F. M. Peeters, Z. Liu, C. L. Hinkle, S.-H. Oh, P. D. Ye, S. J. Koester, Y. H. Lee, P. Avouris, X. Wang *et al.*, npj 2D Materials and Applications **4**, 29 (2020).

[38] X. Zhao, C. Yang, T. Wang, X. Ma, S. Wei, and C. Xia, RSC Adv. **7**, 52747 (2017).

[39] R. M. Dreizler and C. S. Lüdde, A safari through density functional theory, in *Exciting Interdisciplinary Physics: Quarks and Gluons / Atomic Nuclei / Relativity and Cosmology / Biological Systems* (Springer International Publishing, Heidelberg, 2013), pp. 465–478.

[40] R. Asahi, W. Mannstadt, and A. J. Freeman, Phys. Rev. B **59**, 7486 (1999).

[41] J. P. Perdew, K. Burke, and M. Ernzerhof, Phys. Rev. Lett. **77**, 3865 (1996).

[42] J. Heyd, G. E. Scuseria, and M. Ernzerhof, J. Chem. Phys. **118**, 8207 (2003).

[43] A. D. Becke, J. Chem. Phys. **98**, 1372 (1993).

[44] C. Adamo and V. Barone, J. Chem. Phys. **110**, 6158 (1999).

[45] M. A. Flores, W. Orellana, and E. Menéndez-Proupin, Phys. Rev. B **98**, 155131 (2018).

[46] N. Q. Su, Z. Zhu, and X. Xu, Proc. Natl. Acad. Sci. **115**, 2287 (2018).

[47] A. Seidl, A. Görling, P. Vogl, J. A. Majewski, and M. Levy, Phys. Rev. B **53**, 3764 (1996).

[48] P. Liu, C. Franchini, M. Marsman, and G. Kresse, J. Phys.: Condens. Matter **32**, 015502 (2020).

[49] J. H. Skone, M. Govoni, and G. Galli, Phys. Rev. B **93**, 235106 (2016).

[50] J. Toulouse, F. Colonna, and A. Savin, Phys. Rev. A **70**, 062505 (2004).

[51] J. H. Skone, M. Govoni, and G. Galli, Phys. Rev. B **89**, 195112 (2014).

[52] J. Heyd, J. E. Peralta, G. E. Scuseria, and R. L. Martin, J. Chem. Phys. **123**, 174101 (2005).

[53] T. M. Henderson, B. G. Janesko, and G. E. Scuseria, J. Chem. Phys. **128**, 194105 (2008).

[54] J. K. Ellis, M. J. Lucero, and G. E. Scuseria, Appl. Phys. Lett. **99**, 261908 (2011).

[55] T. Yanai, D. P. Tew, and N. C. Handy, Chem. Phys. Lett. **393**, 51 (2004).

[56] R. H. Hertwig and W. Koch, Chem. Phys. Lett. **268**, 345 (1997).

[57] J. P. Perdew, M. Ernzerhof, and K. Burke, J. Chem. Phys. **105**, 9982 (1996).

[58] M. A. L. Marques, J. Vidal, M. J. T. Oliveira, L. Reining, and S. Botti, Phys. Rev. B **83**, 035119 (2011).

[59] T. Shimazaki and T. Nakajima, J. Chem. Phys. **142**, 074109 (2015).

[60] T. Shimazaki and T. Nakajima, J. Chem. Phys. **141**, 114109 (2014).

[61] T. Shimazaki and T. Nakajima, Phys. Chem. Chem. Phys. **18**, 27554 (2016).

[62] S. Refaely-Abramson, S. Sharifzadeh, M. Jain, R. Baer, J. B. Neaton, and L. Kronik, Phys. Rev. B **88**, 081204(R) (2013).

[63] T. Shimazaki and Y. Asai, Chem. Phys. Lett. **466**, 91 (2008).

[64] F. Bechstedt, R. Del Sole, G. Cappellini, and L. Reining, Solid State Commun. **84**, 765 (1992).

[65] T. Shimazaki and Y. Asai, J. Chem. Phys. **130**, 164702 (2009).

[66] T. Shimazaki and Y. Asai, J. Chem. Phys. **132**, 224105 (2010).

[67] D. Koller, P. Blaha, and F. Tran, J. Phys.: Condens. Matter **25**, 435503 (2013).

[68] Z. D. Pozun and G. Henkelman, J. Chem. Phys. **134**, 224706 (2011).

[69] J. C. Conesa, J. Phys. Chem. C **116**, 18884 (2012).

[70] A. Alkauskas, P. Broqvist, F. Devynck, and A. Pasquarello, Phys. Rev. Lett. **101**, 106802 (2008).

[71] A. Alkauskas, P. Broqvist, and A. Pasquarello, physica status solidi (b) **248**, 775 (2011).

[72] P. Broqvist, A. Alkauskas, and A. Pasquarello, physica status solidi (a) **207**, 270 (2010).

[73] W. Kohn and L. J. Sham, Phys. Rev. **140**, A1133 (1965).

[74] G. Kresse and J. Furthmüller, Comput. Mater. Sci. **6**, 15 (1996).

[75] G. Kresse and J. Furthmüller, Phys. Rev. B **54**, 11169 (1996).

[76] P. E. Blöchl, Phys. Rev. B **50**, 17953 (1994).

[77] G. Kresse and D. Joubert, Phys. Rev. B **59**, 1758 (1999).

[78] S. Grimme, J. Comput. Chem. **27**, 1787 (2006).

[79] M. Dion, H. Rydberg, E. Schröder, D. C. Langreth, and B. I. Lundqvist, Phys. Rev. Lett. **92**, 246401 (2004).

[80] H. J. Monkhorst and J. D. Pack, Phys. Rev. B **13**, 5188 (1976).

[81] A. Laturia, M. L. Van de Put, and W. G. Vandenberghe, npj 2D Materials and Applications **2**, 6 (2018).

[82] X. Zhao, T. Wang, S. Wei, X. Dai, and L. Yang, J. Alloys Compd. **695**, 2048 (2017).

[83] L. Sun, W. Zhou, Y. Liu, D. Yu, Y. Liang, and P. Wu, Appl. Surf. Sci. **389**, 484 (2016).

[84] D. Han, W. Ming, H. Xu, S. Chen, D. Sun, and M.-H. Du, Phys. Rev. Applied **12**, 034038 (2019).

[85] S. Chowdhury, P. Venkateswaran, and D. Somvanshi, Superlattices Microstruct. **148**, 106746 (2020).

[86] See Supplemental Material at http://link.aps.org/supplemental/10.1103/PhysRevB.105.195205 for additional information on the secondary phases generated by the transition metal atoms with sulfur atom and their enthalpy of formation, absorption spectra of doped SnS2 systems. which are metals and variation of absorption spectra of Fe-doped monolayer SnS2 with different Fe concentration, dielectric constant and band gap values of TM-doped bulk and monolayer SnS2 semiconductor systems calculated using the self-consistent dielectric-dependent HSE06 and PBE0 functionals.

[87] A. Jain, S. P. Ong, G. Hautier, W. Chen, W. D. Richards, S. Dacek, S. Cholia, D. Gunter, D. Skinner, G. Ceder, and K. A. Persson, APL Mater. **1**, 011002 (2013).

[88] B. Ram and A. K. Singh, Phys. Rev. B **95**, 075134 (2017).

[89] L. A. Burton, D. Colombara, R. D. Abellon, F. C. Grozema, L. M. Peter, T. J. Savenije, G. Dennler, and A. Walsh, Chem. Mater. **25**, 4908 (2013).

[90] J. M. Gonzalez and I. I. Oleynik, Phys. Rev. B **94**, 125443 (2016).

[91] G. Domingo, R. S. Itoga, and C. R. Kannewurf, Phys. Rev. **143**, 536 (1966).

[92] Y. Kumagai, L. A. Burton, A. Walsh, and F. Oba, Phys. Rev. Applied **6**, 014009 (2016).

[93] C. Bacaksiz, S. Cahangirov, A. Rubio, R. T. Senger, F. M. Peeters, and H. Sahin, Phys. Rev. B **93**, 125403 (2016).

[94] M. Toh, K. Tan, F. Wei, K. Zhang, H. Jiang, and C. Kloc, J. Solid State Chem. **198**, 224 (2013).

[95] J. E. Padilha, H. Peelaers, A. Janotti, and C. G. Van de Walle, Phys. Rev. B **90**, 205420 (2014).

[96] C. D. Lokhande, J. Phys. D **23**, 1703 (1990).

[97] Y. Sun, H. Cheng, S. Gao, Z. Sun, Q. Liu, Q. Liu, F. Lei, T. Yao, J. He, S. Wei, and Y. Xie, Angew. Chem., Int. Ed. **51**, 8727 (2012).

[98] Y. Cai, G. Zhang, and Y.-W. Zhang, Sci. Rep. **4**, 6677 (2015).

[99] S. Das, W. Zhang, M. Demarteau, A. Hoffmann, M. Dubey, and A. Roelofs, Nano Lett. **14**, 5733 (2014).

[100] M. Gerosa, C. E. Bottani, L. Caramella, G. Onida, C. Di Valentin, and G. Pacchioni, Phys. Rev. B **91**, 155201 (2015).

[101] C. H. Chen, W. Fabian, F. C. Brown, K. C. Woo, B. Davies, B. DeLong, and A. H. Thompson, Phys. Rev. B **21**, 615 (1980).

[102] D. R. Allan, A. A. Kelsey, S. J. Clark, R. J. Angel, and G. J. Ackland, Phys. Rev. B **57**, 5106 (1998).

[103] P. C. Klipstein and R. H. Friend, J. Phys. C **17**, 2713 (1984).

[104] J. J. Barry, H. P. Hughes, P. C. Klipstein, and R. H. Friend, J. Phys. C **16**, 393 (1983).

[105] F. R. Shepherd and P. M. Williams, J. Phys. C **7**, 4416 (1974).

[106] G. A. Benesh, A. M. Woolley, and C. Umrigar, J. Phys. C **18**, 1595 (1985).

[107] C. M. Fang, R. A. de Groot, and C. Haas, Phys. Rev. B **56**, 4455 (1997).

[108] Z. Y. Wu, G. Ouvrard, S. Lemaux, P. Moreau, P. Gressier, F. Lemoigno, and J. Rouxel, Phys. Rev. Lett. **77**, 2101 (1996).

[109] Z. Y. Wu, F. Lemoigno, P. Gressier, G. Ouvrard, P. Moreau, J. Rouxel, and C. R. Natoli, Phys. Rev. B **54**, R11009 (1996).

[110] Z. Y. Wu, G. Ouvrard, P. Moreau, and C. R. Natoli, Phys. Rev. B **55**, 9508 (1997).

[111] S. Sharma, T. Nautiyal, G. S. Singh, S. Auluck, P. Blaha, and C. Ambrosch-Draxl, Phys. Rev. B **59**, 14833 (1999).

[112] A. H. Reshak and S. Auluck, Phys. Rev. B **68**, 245113 (2003).

[113] E. E. Abbott, J. W. Kolis, N. D. Lowhorn, W. Sams, and T. M. Tritt, MRS Online Proc. Lib. **793**, 322 (2003).

[114] C. A. Kukkonen, W. J. Kaiser, E. M. Logothetis, B. J. Blumenstock, P. A. Schroeder, S. P. Faile, R. Colella, and J. Gambold, Phys. Rev. B **24**, 1691 (1981).

[115] S. Suga, C. Tusche, Y. ichiro Matsushita, M. Ellguth, A. Irizawa, and J. Kirschner, New J. Phys. **17**, 083010 (2015).

[116] K. Hu, D. Wang, W. Zhao, Y. Gu, K. Bu, J. Pan, P. Qin, X. Zhang, and F. Huang, Inorg. Chem. **57**, 3956 (2018).

[117] K. M. Kim, B. S. Kwak, S. Kang, and M. Kang, Int. J. Photoenergy **2014**, 479508 (2014).

[118] C. Xia, J. An, T. Wang, S. Wei, and Y. Jia, Acta Mater. **72**, 223 (2014).

[119] P. Wahnón, J. C. Conesa, P. Palacios, R. Lucena, I. Aguilera, Y. Seminovski, and F. Fresno, Phys. Chem. Chem. Phys. **13**, 20401 (2011).

[120] O. Yassin, A. Abdelaziz, and A. Jaber, Mater. Sci. Semicond. Process. **38**, 81 (2015).

[121] L. Lin, Y. Chen, H. Tao, L. Yao, J. Huang, L. Zhu, M. Lou, R. Chen, L. Yan, and Z. Zhang, Phys. Chem. Chem. Phys. **23**, 6574 (2021).

[122] M. Taleblou, E. Borhani, B. Yarmand, and A. R. Kolahi, Mater. Res. Expr. **6**, 025908 (2018).

[123] L. Sun, W. Zhou, Y. Liu, D. Yu, Y. Liang, and P. Wu, RSC Adv. **6**, 3480 (2016).

[124] L. Sun, W. Zhou, Y. Liang, L. Liu, and P. Wu, Comput. Mater. Sci. **117**, 489 (2016).

[125] A. S. Alqarni, B. Alsobhi, A. Elabbar, and O. Yassin, Mater. Sci, Semicond. Process. **59**, 18 (2017).

[126] M. Jiang, Y. Huang, W. Sun, and X. Zhang, J. Mater. Sci. **54**, 13715 (2019).

[127] G. Kiruthigaa, C. Manoharan, C. Raju, S. Dhanapandian, and V. Thanikachalam, Mater. Sci, Semicond. Process. **26**, 533 (2014).

[128] H. Ullah, M. Noor-A-Alam, and Y.-H. Shin, J. Am. Ceram. Soc. **103**, 391 (2020).

[129] W. Zhao, Z. Wei, L. Zhang, X. Wu, and X. Wang, Mater. Sci, Semicond. Process. **88**, 173 (2018).

[130] H. Bouzid, R. Sahoo, S. J. Yun, K. Singh, Y. Jin, J. Jiang, D. Yoon, H. Y. Song, G. Kim, W. Choi, Y.-M. Kim, and Y. H. Lee, Adv. Funct. Mater. **31**, 2102560 (2021).

[131] B. Li, T. Xing, M. Zhong, L. Huang, N. Lei, J. Zhang, J. Li, and Z. Wei, Nature Commun. **8**, 1958 (2017).

[132] X. Ma, X. Zhao, and T. Wang, RSC Adv. **6**, 69758 (2016).

[133] A. Ali, J.-M. Zhang, I. Muhammad, I. Shahid, I. Ahmad, M. U. Rehman, I. Ahmad, and F. Kabir, Phys. E **134**, 114842 (2021).

[134] Y. Gong, H. Yuan, C.-L. Wu, P. Tang, S.-Z. Yang, A. Yang, G. Li, B. Liu, J. van de Groep, M. L. Brongersma, M. F. Chisholm, S.-C. Zhang, W. Zhou, and Y. Cui, Nature Nanotechnol. **13**, 294 (2018).

[135] G. Mohan Kumar, F. Xiao, P. Ilanchezhiyan, S. Yuldashev, A. Madhan Kumar, H. Cho, D. Lee, and T. Kang, Appl. Surf. Sci. **455**, 446 (2018).

[136] G. Mohan Kumar, P. Ilanchezhiyan, H. D. Cho, S. Yuldashev, H. C. Jeon, D. Y. Kim, and T. W. Kang, Nanomaterials **9**, 924 (2019).

[137] C. M. I. Okoye, J. Phys.: Condens. Matter **15**, 5945 (2003).

[138] L. Li, Q. Lv, Y. Li, L. Li, Y. Zhao, J. Mao, D. Shao, R. Tan, S. Shi, and T. Chen, Catal. Lett. **150**, 2792 (2020).

[139] S. Saha, T. P. Sinha, and A. Mookerjee, Phys. Rev. B **62**, 8828 (2000).

[140] X. Zhang, W. Wang, Q. Zeng, and H. Li, Solid State Commun. **150**, 360 (2010).

[141] P. Cudazzo, I. V. Tokatly, and A. Rubio, Phys. Rev. B **84**, 085406 (2011).

[142] L. V. Keldysh, Pis'ma Zh. Eksp. Teor. Fiz. **29**, 716 (1979) [JETP Lett. **29**, 658 (1979)].

[143] E. Prada, J. V. Alvarez, K. L. Narasimha-Acharya, F. J. Bailen, and J. J. Palacios, Phys. Rev. B **91**, 245421 (2015).

[144] A. Schindlmayr, Eur. J. Phys. **18**, 374 (1997).

[145] S. Arra, R. Babar, and M. Kabir, Phys. Rev. B **99**, 045432 (2019).
[146] Wolfram Research, Inc., Mathematica 10.2, 2015.
[147] V. Wang, N. Xu, J.-C. Liu, G. Tang, and W.-T. Geng, Comput. Phys. Commun. **267**, 108033 (2021).
[148] K. A. Velizhanin and A. Saxena, Phys. Rev. B **92**, 195305 (2015).
[149] J. Z. Ou, W. Ge, B. Carey, T. Daeneke, A. Rotbart, W. Shan, Y. Wang, Z. Fu, A. F. Chrimes, W. Wlodarski, S. P. Russo, Y. X. Li, and K. Kalantar-zadeh, ACS Nano **9**, 10313 (2015).